

Phase Coexistence and Structural Dynamics of Redox Metal Catalysts Revealed by Operando TEM

Xing Huang,* Travis Jones, Alexey Fedorov, Ramzi Farra, Christophe Copéret, Robert Schlögl, and Marc-Georg Willinger*

Metal catalysts play an important role in industrial redox reactions. Although extensively studied, the state of these catalysts under operating conditions is largely unknown, and assignments of active sites remain speculative. Herein, an operando transmission electron microscopy study is presented, which interrelates the structural dynamics of redox metal catalysts to their activity. Using hydrogen oxidation on copper as an elementary redox reaction, it is revealed how the interaction between metal and the surrounding gas phase induces complex structural transformations and drives the system from a thermodynamic equilibrium toward a state controlled by the chemical dynamics. Direct imaging combined with the simultaneous detection of catalytic activity provides unparalleled structure–activity insights that identify distinct mechanisms for water formation and reveal the means by which the system self-adjusts to changes of the gas-phase chemical potential. Density functional theory calculations show that surface phase transitions are driven by chemical dynamics even when the system is far from a thermodynamic phase boundary. In a bottom-up approach, the dynamic behavior observed here for an elementary reaction is finally extended to more relevant redox reactions and other metal catalysts, which underlines the importance of chemical dynamics for the formation and constant re-generation of transient active sites during catalysis.

urgently needed transition to a more sustainable society in general, and chemical industry in particular.^[1,2] However, despite intensive research, our present understanding of processes governing activation, stable performance, aging, deactivation and regeneration of catalysts is insufficient to cope with this challenge.^[3–14] Consequently, and regardless of our advances in synthesis and characterization methods, empirical discovery of new catalysts is still the norm. This is a very inefficient, time-consuming, and overall unsatisfying endeavor. Claims about tailored design of optimal catalysts can only be fulfilled once an atomistic understanding of the structure–activity correlation of working catalysts is established. This requires that we first understand how the chemical potential of reactants influences the state of a catalyst, and how these gas-phase- and temperature-induced modifications feed back into, or evolve during, the catalytic process. In order to shed more light on the interplay between catalyst and reactive species and to follow processes that lead to the emergence of catalytic activity, real-

space and real-time observation of the active catalyst at high spatial resolution is required.^[15,16]


Since the ground-breaking work of Ruska,^[17] in situ transmission electron microscopy (TEM) has transformed into a

1. Introduction

The development of improved catalysts for resource-efficient processes and a CO₂ neutral energy supply is vital for an

Prof. X. Huang, Dr. M.-G. Willinger
Scientific Center for Optical and Electron Microscopy
ETH Zurich
Otto-Stern-Weg 3, Zurich 8093, Switzerland
E-mail: marc.willinger@scopem.ethz.ch

Prof. X. Huang
College of Chemistry
Fuzhou University
Fuzhou 350116, P. R. China
E-mail: xinghuang@fzu.edu.cn

 The ORCID identification number(s) for the author(s) of this article can be found under <https://doi.org/10.1002/adma.202101772>.

© 2021 The Authors. Advanced Materials published by Wiley-VCH GmbH. This is an open access article under the terms of the Creative Commons Attribution-NonCommercial-NoDerivs License, which permits use and distribution in any medium, provided the original work is properly cited, the use is non-commercial and no modifications or adaptations are made.

DOI: 10.1002/adma.202101772

Prof. X. Huang, Prof. C. Copéret
Department of Chemistry and Applied Biosciences
ETH Zurich
Vladimir-Prelog-Weg 1-5, Zurich 8093, Switzerland
Prof. X. Huang, Dr. T. Jones, Dr. R. Farra, Prof. R. Schlögl,
Dr. M.-G. Willinger
Fritz-Haber Institute of Max-Planck Society
Faradayweg 4-6, 14195 Berlin, Germany
Dr. A. Fedorov
Department of Mechanical and Process Engineering
ETH Zurich
Leonhardstrasse 21, 8092 Zurich, Switzerland
Prof. R. Schlögl
Department Heterogeneous Reactions
Max Planck Institute for Chemical Energy Conversion
45470 Mülheim an der Ruhr, Germany

powerful method for the investigation of gas–solid interactions, delivering valuable insights about adsorbent-induced surface structuring,^[18–21] particle shape reconstruction,^[22–24] and phase changes.^[25,26] The recent development of nanoreactors with silicon-based micro-electromechanical systems (MEMS) technology has further enabled in situ TEM studies of catalysts at pressures up to ≈ 1 bar and temperatures up to 1000 °C.^[27,28] This bridges the pressure gap for many relevant reactions and enables a transformative shift from imaging of quasiequilibrium states to observation of nonequilibrium dynamics. Through the combination of real-time imaging with on-line mass spectrometry (MS) it is then possible to relate reaction induced dynamics to variations in gas-phase composition and catalytic activity. Thus, structure–property correlations can be investigated while a catalyst is in its working state.^[22]

Industrial redox catalysis typically relies on transition metals, in particular copper, which is used as an active component in catalysts for CO₂ reduction,^[3,29–31] ethylene epoxidation,^[4,5] methanol oxidation,^[32,33] and the water gas shift reaction.^[34,35] However, an atomistic description of the state of copper under redox conditions in these catalysts is still unavailable, although integral spectroscopic data obtained under low-pressure conditions indicate that more than one phase is often present in the active catalyst.^[13,32,36]

Building on earlier electron microscopy investigations on oxidation and reduction of copper,^[37–40] we present a detailed study of the working state of several redox catalysts and redox reactions in the following sections. First, we focus on a high-resolution study of Cu during the hydrogen oxidation reaction (HOR) revealing fundamentals of catalyst dynamics under reactive conditions. Yielding only water as a product, the complexity related to possible electron-beam-induced processes, especially at high magnification and relatively high electron beam dose rates, is reduced considerably when studying HOR. Therefore, this reaction offers the opportunity to gain detailed atomistic insights into the interaction between the catalyst and the gas phase. Our study assessed systematically the effects of temperature and gas-phase conditions, and revealed how the chemical potential of the gas phase defines the phase, size, and shape of catalyst particles, driving the system into a nonequilibrium dynamic state during catalysis. Due to the simultaneous detection of catalytic conversion, we are able to relate directly the observed dynamics and surface structures to catalytic activity. Density functional theory (DFT) calculations were performed to rationalize further the observed phase transitions and coexistence of phases, which are driven by chemical dynamics that occur under conditions far from the thermodynamic equilibrium. The described phase transformations are the basis for oscillatory behavior, which has been observed in several Cu-catalyzed reactions and emerges when transformations are spatially coupled.^[36,40] Finally, we extend these observations to other redox reactions and metal catalysts by demonstrating that copper and palladium show similar redox dynamics in the active state during methanol oxidation and methane oxidation reactions, respectively. Thus, the structural dynamics, revealed fully in the in situ movies accompanying this paper, is a fundamental feature of redox catalysis with major general implications for mechanistic and structural studies of heterogeneous catalysts.

2. Results and Discussion

2.1. Hydrogen Oxidation Reaction on Copper

Copper nanoparticles of 50–200 nm (Figure S1, Supporting Information) were loaded in the in situ gas-flow reactor (DENSolutions Climate system; Figure S2, Supporting Information). At the beginning of each in situ experiment, the Cu particles were reduced in hydrogen (see Figures S3 and S4 in the Supporting Information for details).

2.1.1. Structural Changes of Cu⁰ in a Redox Atmosphere

Starting with fully reduced Cu particles, we first studied the response of Cu when the conditions change from reducing to redox. This was done by slowly adding oxygen to a gas flow of 20% H₂ and 80% He until a set ratio of 2% O₂, 20% H₂, and 78% He was reached ($p_{\text{O}_2} = 5.7$ mbar, $p_{\text{H}_2} = 57$ mbar). Throughout the process, the temperature of the sample was held constant, depending on the experiment, either at 400 or 500 °C. Images were recorded at low magnification in order to prevent electron-beam-induced artifacts (see the Experimental Section in the Supporting Information for details regarding prevention of electron beam artifacts). As can be seen in **Figure 1** and in **Movies S1 and S2** (Supporting Information), the addition of oxygen induces fragmentation of the reduced Cu particles. The process, which shows similarities to metal dusting,^[41] starts at the surface and progressively propagates into the bulk. Note that the structural disintegration leads to particles of a certain size regime, which implies that Cu particles do not infinitely fragment into ever smaller particles (vide infra). Note that a similar structural transformation was observed in control experiments in an environmental scanning electron microscope (ESEM). The exposure of a polycrystalline Cu foil to the 10:1 H₂/O₂ gas feed ratio ($p_{\text{O}_2} + p_{\text{H}_2} = 0.2$ mbar) at 400 °C leads to the progressive fragmentation of the foil surface, resulting in small particles with rich structural dynamics (**Movie S3**, Supporting Information). Although the experiments in the ESEM were performed at 0.2 mbar and thus, 4 orders of magnitude lower than total pressure, it is apparent that the bulk Cu foil shows a very similar behavior as the Cu nanoparticles.

In situ TEM images of Cu nanoparticles recorded at intermediate magnification reveal that the resulting smaller particles show rich structural dynamics, which are associated with reconstruction and random motion, as well as particle sintering and splitting (**Figure 2A–L**; **Movie S4**, Supporting Information). For the identification of the involved phases, we performed in situ selected-area electron diffraction (SAED), which provides integral information at minimal beam exposure. It showed dynamically appearing and disappearing diffraction spots, and confirmed the presence of metallic copper and Cu₂O as the sole oxide phase (see **Figure 2M**; **Figure S5** and **Movie S5**, Supporting Information). This, together with the structural dynamics and the occurrence of features with light contrast, reflects the constant competition between oxide growth and reduction. The structural dynamics are thus a consequence of chemical dynamics, characterized by phase coexistence and constant interconversion between Cu⁰ and Cu₂O.

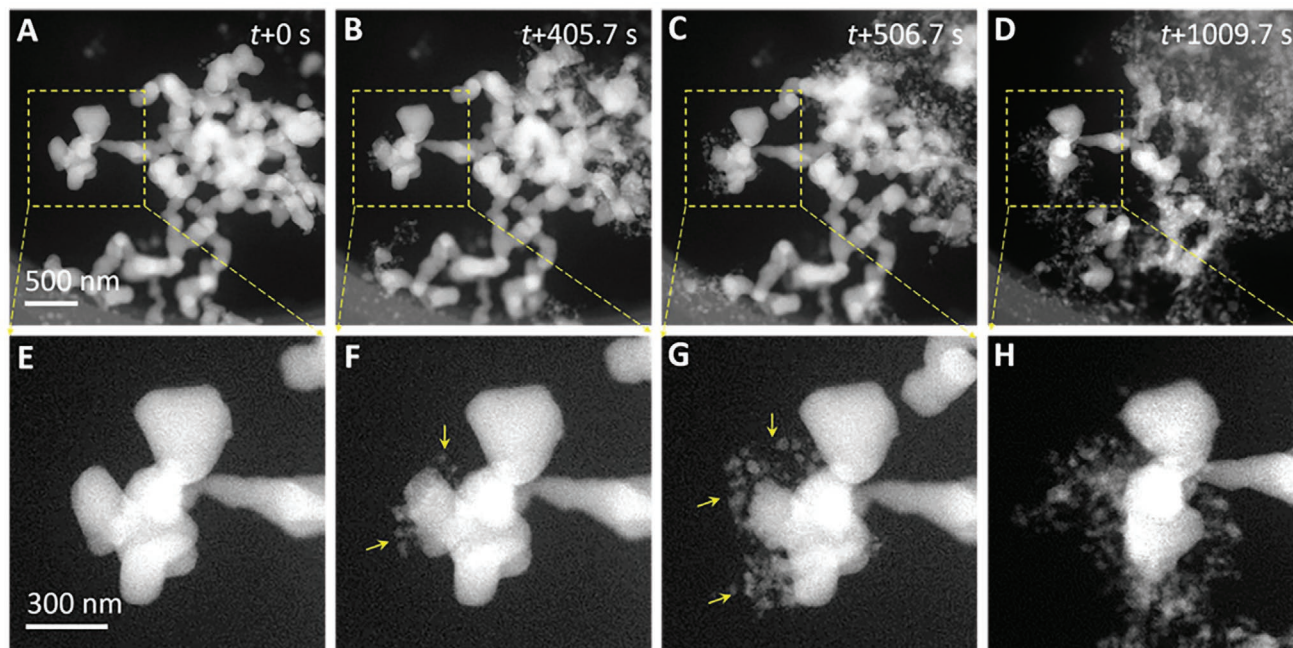


Figure 1. Fragmentation of Cu^0 particles in a redox atmosphere. A–H) In situ observation of structural changes during the addition of O_2 (2%) to a flow of H_2 (20%) in He at $400\text{ }^\circ\text{C}$.

This is also confirmed by in situ high-resolution imaging (Figure 2N), which was performed after verification that the chosen imaging conditions do not interfere with the observed dynamics (for more information, see the Experimental Section in the Supporting Information). Real-time imaging shows that the structural dynamics lead to the establishment of a certain size regime (Figure S6, Supporting Information) that is determined by a balance between particle sintering and splitting. At the lower end of the size distribution, particle sintering is more prominent, whereas larger particles are more likely to split. The latter seems to happen exclusively at the elongated tail-like outgrowth during the reduction, when the reduction process is too fast for an ordered retraction of the copper to the main particle (Movie S6, Supporting Information). This results in a fragmentation of the tail-like outgrowth and formation of one or more smaller metallic nanoparticles. Interestingly, particles are not fully converted to Cu_2O during the oxidizing phase of the oscillatory redox dynamics. Even at the turning point between oxidation and reduction, there is always a metallic fraction remaining, suggesting that the metal and/or metal-oxide interfaces play an important role in the activation of reactants. Overall, the resulting size regime and phase composition depend on the chemical potential of the gas phase, as will be shown in the following.

2.1.2. Effect of the Chemical Potential

Effect of Temperature: To study the effect of temperature ($300\text{--}750\text{ }^\circ\text{C}$) on the observed redox dynamics, we first decreased the temperature from 500 to $300\text{ }^\circ\text{C}$ ($p_{\text{H}_2} = 57\text{ mbar}$, $p_{\text{O}_2} = 5.7\text{ mbar}$). During the temperature decrease, we observed the growth of oxide dendrites, which reflects the increasing

oxidation potential. At the same time, owing to the slower kinetics of the redox reaction at lower temperatures, a reduction of the structural dynamics was observed (Movie S7, Supporting Information). Note that the changes observed during cooling suggest that ex situ, postcatalytic characterization of catalyst can give misleading results concerning the working state of a catalyst. During heating from 300 to $750\text{ }^\circ\text{C}$, the system passes through a regime of increased dynamics ($550\text{ }^\circ\text{C}$) that are characterized by translational motion and restructuring due to oxide growth and reduction until it finally reaches a state that is less dynamic and dominated by metallic copper at $750\text{ }^\circ\text{C}$ (Figure 3A–D; Movie S8, Supporting Information). With increasing relative fraction of the metallic phase, particle sintering gradually overtakes particle splitting. As a consequence, the average particle size grows. Lattice fringe imaging confirms the high portion of Cu_2O at low temperature and the predominance of metallic copper at high temperature (see Figure 3E,F and Figure S7 in the Supporting Information, respectively). Phase analysis by integral SAED reveals the relation between phase composition and temperature. As shown in Figure 3G,H, the relative fraction of the oxide phase decreases with increasing temperature. However, there is a clear local maximum in the oxide content at around $550\text{ }^\circ\text{C}$, which coincides with the regime of highest structural dynamics and, as will be shown later, with high catalytic activity. Thus, although the trend in the oxide content reflects the decreasing chemical potential of oxygen with increasing temperature,^[4,42] we observe an interesting exception of this general trend at the temperature around $550\text{ }^\circ\text{C}$ (for the chosen H_2/O_2 ratio of 10:1).

Effect of the Gas-Phase Composition: To study the influence of the gas-phase composition on the structural dynamics, we gradually decreased the H_2/O_2 ratio from 10/1 ($p_{\text{H}_2} = 57\text{ mbar}$, $p_{\text{O}_2} = 5.7\text{ mbar}$) to 5/1 ($p_{\text{H}_2} = 31.7\text{ mbar}$, $p_{\text{O}_2} = 6.3\text{ mbar}$) at

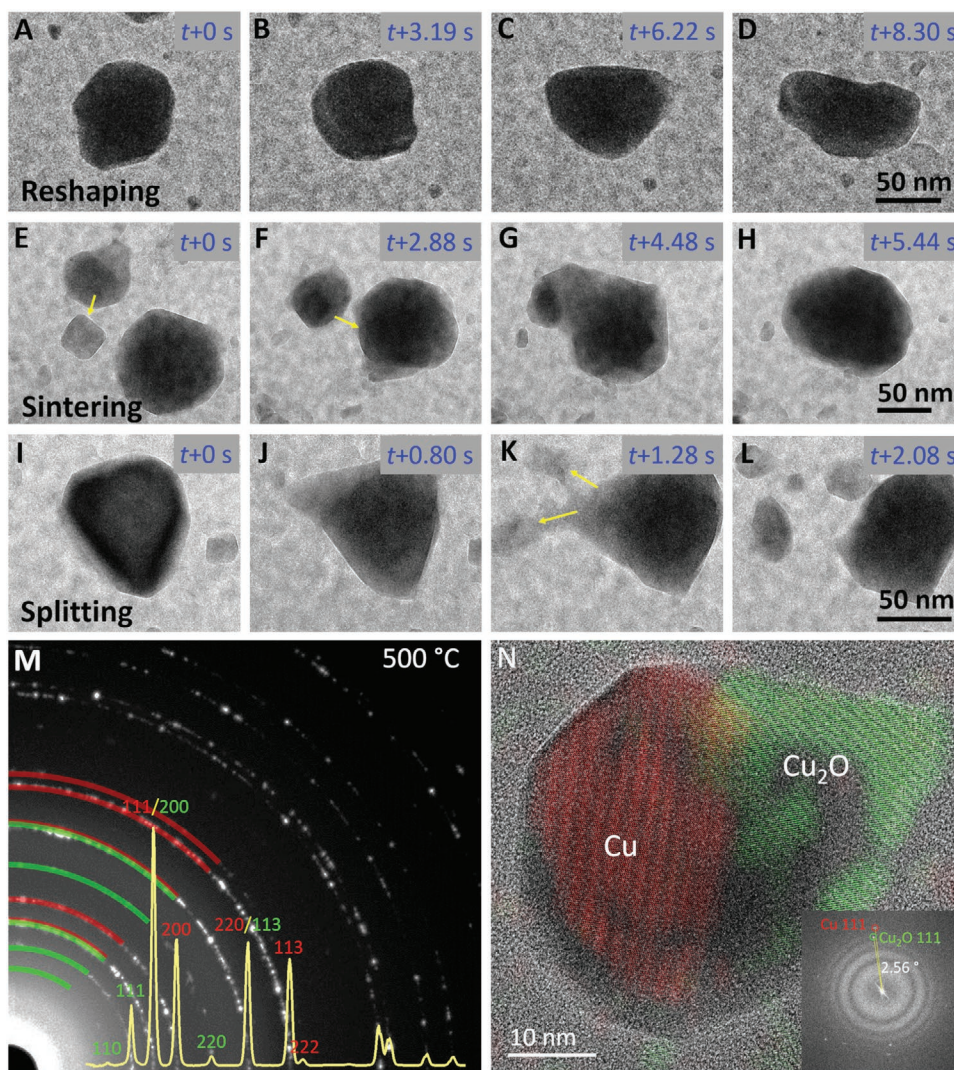


Figure 2. Redox dynamics and structural analysis of Cu. A–L) In situ TEM observations of catalyst reshaping (A–D), sintering (E–H), and splitting (I–L) at a H_2/O_2 ratio of 10/1 ($P_{\text{H}_2} = 57$ mbar, $P_{\text{O}_2} = 5.7$ mbar) and at 500 °C (A–D)/550 °C (E–L) (electron dose rate: $1.5\text{--}6.5 \times 10^3 e \text{ nm}^{-2} \text{ s}^{-1}$). M) Integrated SAED pattern and corresponding radial intensity profile. N) In situ high-resolution TEM (HRTEM) image of a nanoparticle containing a metallic head coherently interfacing with an oxide tail (electron dose rate: $1.4 \times 10^5 e \text{ nm}^{-2} \text{ s}^{-1}$).

500 °C. The relative increase of the oxygen partial pressure leads to a transformation of initially spherical nanoparticles into elongated particles with a head–tail structure (Figure S1I–L; Movie S9, Supporting Information). At the same time, the average particle size declines due to an increased rate of particle splitting, until a new size regime and dynamic equilibrium is established. The resulting elongated particles show a higher fraction of Cu_2O (Figures S8 and S9, Supporting Information) and rich structural dynamics which are described in more details in Figures S10–S12 and Movies S10–S12 (Supporting Information).

We then investigated the effect of temperature under the 5:1 ratio in order to confirm that an increase of the oxygen partial pressure shifts the regime of structural dynamics to higher temperature (Figure S13 and Movie S13, Supporting Information). Indeed, the static state of metallic copper nanoparticles was observed at ≈ 850 °C for a 5:1 ratio (compared to 750 °C at a

10:1 H_2/O_2 ratio). Consequently, the radial profiles of integrated SAED patterns display a similar trend for the Cu_2O (111)/Cu (111) peak ratios as found in the case of the 10:1 ratio, but with a shift of the local maximum in the Cu_2O fraction to higher temperature (Figure S14, Supporting Information).

Real-time observations under varying gas-phase composition and temperature show a clear effect of the gas-phase chemical potential on the average particle size. Since sintering generally occurs between metallic parts of colliding particles (Figures S11 and S12, and Movies S11 and S12, Supporting Information), we observe more sintering and, hence, larger particles at higher hydrogen concentration (at a given temperature). On the other hand, since particle splitting occurs at the oxide outgrowth, particle fragmentation and reduction of the average particle size are observed at increased oxygen chemical potential (compare Figure S1I with Figure S3L). We reiterate these observations because sintering in catalysis is typically considered the

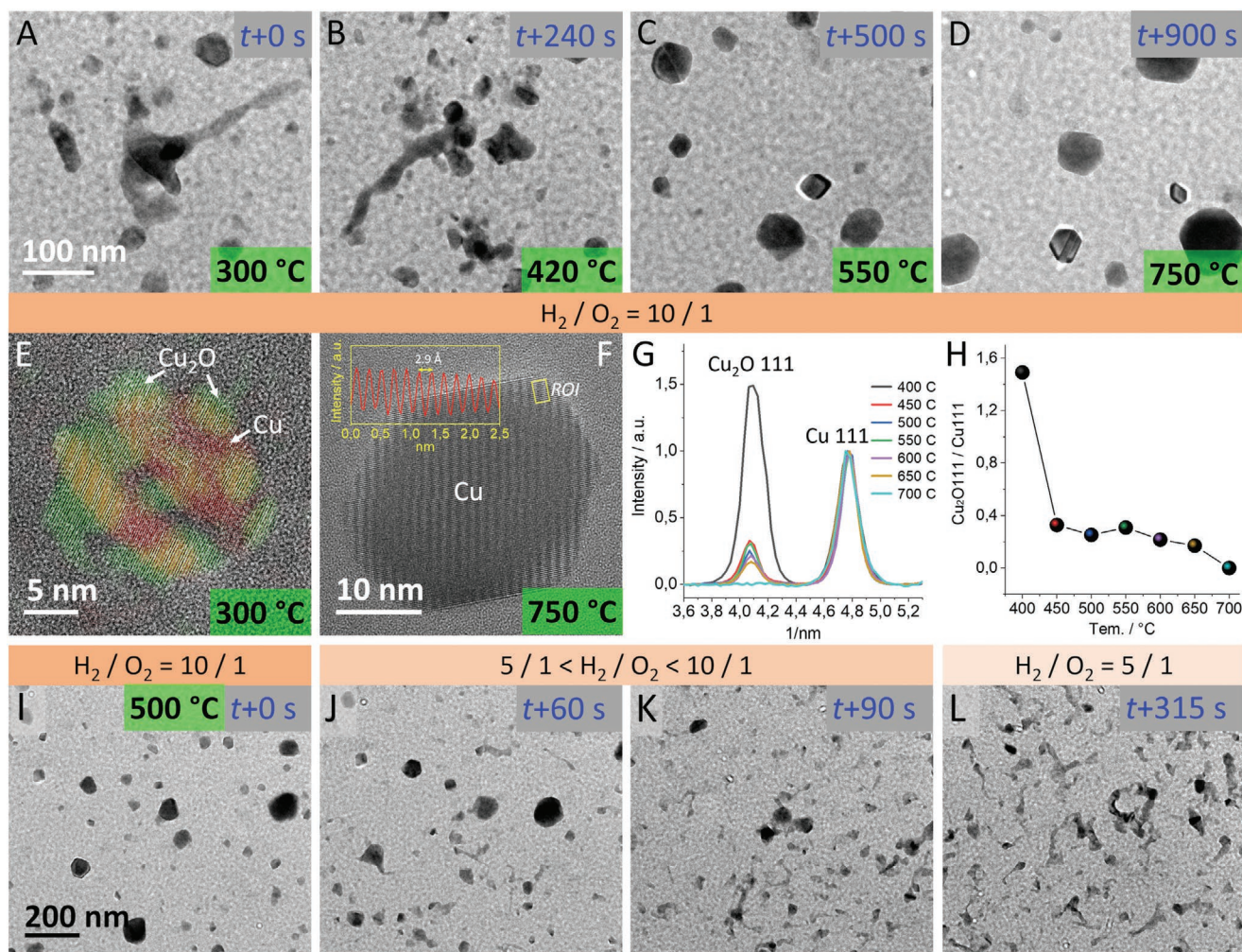


Figure 3. Chemical potential versus structural dynamics of Cu. A–D) In situ TEM observation of dynamics at 300–750 °C and a H_2/O_2 ratio of 10/1 (electron dose rate: $4 \times 10^3 e nm^{-2} s^{-1}$). E, F) Reconstructed HRTEM images taken at 300 and 750 °C (electron dose rates: 8.7×10^4 and $2.6 \times 10^5 e nm^{-2} s^{-1}$, respectively). G) Normalized radial profiles extracted from the integrated SAED patterns and H) radial intensity profile and the abstracted intensity ratio of Cu_2O (111)/Cu (111) as a function of temperature. I–L) In situ observation of copper dynamics during decreasing H_2/O_2 ratio from 10/1 to 5/1 at 500 °C (electron dose rate: $2.5 \times 10^3 e nm^{-2} s^{-1}$).

characteristic of thermally induced processes.^[43,44] Our in situ observations show clearly that redox dynamics make particles mobile and thereby increase substantially the rate of sintering as compared to thermal sintering; yet the sintering under redox conditions is balanced by particle splitting.

2.1.3. Relation between Structural Dynamics and Catalytic Processes

The key asset of in situ/operando tools in catalysis research is their ability to reveal the correlation between gas-phase and temperature-induced dynamic processes, and their relation to catalytic function and activity. Having described how the gas-phase chemical potential alters the initial copper particles, we now turn to analysis of the MS data that were recorded simultaneously with the observations of the structural dynamics by connecting the outline flow of the in situ TEM holder to a quadrupole MS. The collected MS data presented in **Figure 4A**

clearly show the formation of water and simultaneous consumption of oxygen, confirming the catalytic activity of copper. Note that a control experiment using an empty nanoreactor at otherwise identical conditions shows no O_2 consumption or H_2O production over the entire range of experimental temperatures (**Figure 4A**). This result demonstrates the inertness of the reaction cell and associates the oxygen consumption and production of water with the Cu-based catalytic reaction. Importantly, the detection of water and the consumption of oxygen start only above 400 °C, which coincide with the onset of the redox dynamics. The notable increase in water production and oxygen consumption is observed between 500 and 600 °C. This temperature range coincides with the regime of intense structural dynamics discussed earlier (**Figure 3H**; **Figure S15**, Supporting Information). While it is clear that the MEMS-based reaction cell of the in situ TEM holder, which contains only minute amounts of catalyst, is not optimal for quantitative kinetic studies, in the following we correlate observed

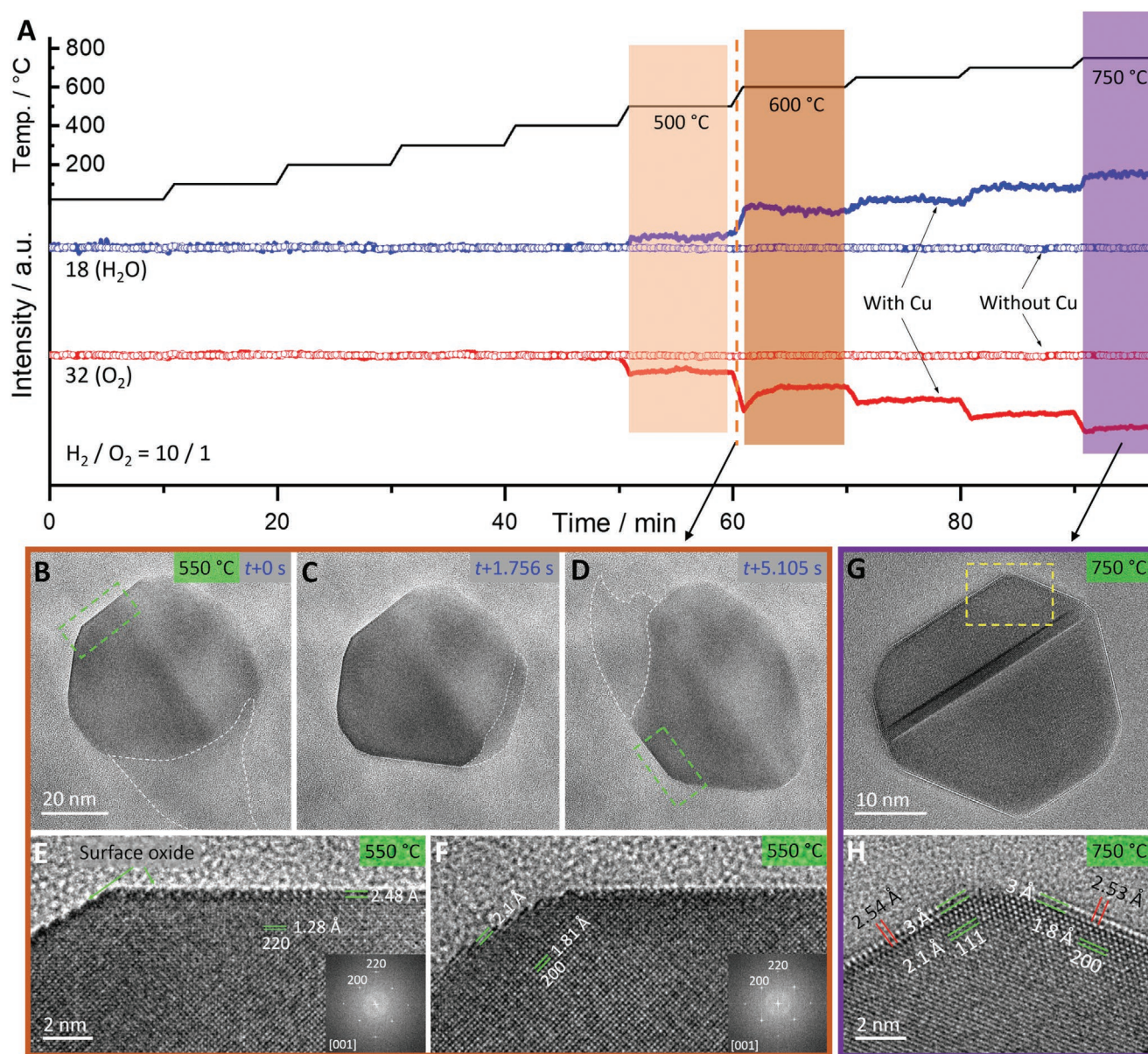


Figure 4. Relation between structural dynamics of Cu and catalytic activity. A) In situ MS data collected from loaded and empty reaction cell at varied temperatures. B–D) Sequential HRTEM images of particle reshaping/restructuring at 550 °C and a H_2/O_2 ratio of 10/1. E,F) Enlarged HRTEM images of the areas indicated by dashed rectangles in (B) and (D). G) HRTEM image, and H) enlarged HRTEM image of the area indicated by the dotted rectangle in (G). (Electron dose rate: $1.3\text{--}4 \times 10^5 e \text{ nm}^{-2} \text{ s}^{-1}$).

structural features and dynamics to possible mechanisms of water formation.

One pathway for the hydrogen oxidation reaction is the reduction of bulk Cu_2O by H_2 . It occurs through adsorption and dissociation of hydrogen on the oxide surface, followed by the reaction with the lattice oxygen to form hydroxyls.^[38,39] At this reaction temperature, dehydroxylation takes place, forming water molecules that desorb from the surface. Therefore, as long as the oscillatory redox phase transitions are ongoing, water will be continuously formed via bulk oxide reduction.^[40,45] The relevance of this process is indicated by the coincidence of the high increase of water formation with the regime of maximal structural dynamics. This reaction

regime furthermore coincides with the local maxima in the Cu_2O content, which was assessed from the Cu_2O (111)/Cu (111) peak ratios in the integral SAED pattern (Figure 3G,H). From these data, we eventually see an effect of the substantial amount of water that is forming. Water can partially decompose on the surface of Cu^0 and contribute, with its 2:1 ratio of H_2 and O_2 , to changing locally the set 10:1 ratio of H_2 and O_2 in the gas feed. Product decomposition thus may promote oxide formation. However, since water formation is also observed at higher temperatures, i.e., beyond the structural dynamics regime and stability of Cu_2O , another HOR mechanism(s) must be in play at these temperatures (vide infra).

The high-resolution images recorded in the redox regime provide atomic details of dynamic reconstructing of a Cu particle at a 10:1 ratio of H₂ and O₂ (Figure 4B–D; Movie S14, Supporting Information). The interconversion between Cu⁰ and Cu₂O involves diffusion of copper and oxygen atoms and dynamic reshaping of particles. An oxide monolayer is observed on the surface of the metallic portion of the particles, as indicated by the extended lattice spacing (Figure 4E,F). Due to the relatively fast structural dynamics, capturing this thin layer is challenging. It is only visible when seen edge on (that is, when the oxide layer is parallel to the beam direction) and difficult to detect because of the weak contrast and the blurring, which is due to the diffuse electron scattering by the SiN_x windows of the MEMS chips and the gas phase. In this reaction regime, constant refaceting and reshaping are accompanied by the growth and reduction of bulk oxide structures (tail or islands) at different locations on the surface of the Cu particles. Oxygen atoms of this layer can either be harvested by hydrogen, toward direct H₂O formation, or serve as an oxygen reservoir or nucleation site for the Cu₂O growth. Thus, direct H₂O formation from the oxygen monolayer is a competing route for HOR, along with the bulk oxidation and Cu₂O reduction pathway to water formation. Constant reconstruction and reconfiguration reflect the competition between the two pathways. The surface oxide layer is observed even at 750 °C at a H₂/O₂ ratio of 10/1 (Figures S15 and S16, Supporting Information). Under these conditions, the bulk oxide growth no longer occurs (see Movie S15 in the Supporting Information) and therefore, the detected activity in this temperature regime is related to the surface oxide layer. The assessment by TEM of the atomistic processes involved in this layer during catalysis is hampered due to fast movement of individual atoms as well as the limited time resolution and constraints related to the applicable beam dose rate. However, structural features of the monolayer oxide can be imaged on various facets (Figure 4G,H). Based on earlier literature reports and acquired electron energy loss spectroscopy (EELS) data (Figure S17, Supporting Information), we assign this monolayer oxide to a Cu₂O-like surface structure^[37,46] rather than to an oxygen-chemisorbed layer.^[47–51] Yet the in-plane spacing deduced from the images indicates a compressed state in the Cu₂O-like surface structure as compared to regular Cu₂O. This is expected for an oxide lattice that is larger than the metal lattice on which it is based.^[37] Contrary to earlier studies based on in situ X-ray techniques,^[32,33,52] we did not find any evidence for subsurface oxygen besides this surface layer. Noteworthy, a similar surface oxide layer, referred to as O_γ, was proposed for silver under conditions of methanol oxidation, and is thought to be relevant for formaldehyde formation.^[10] Similar to the case of copper, the surface oxygen O_γ species on silver are highly stable.^[53]

2.1.4. Computational Modeling

In order to elucidate the possible catalytic mechanism that involves the above-described surface oxide layer, we performed computational modeling based on DFT calculations (for details, see the “Computational Methods” in the Supporting Information). Cu₂O and five surface structures on the Cu (111) surface

were identified when the catalyst is under constrained equilibrium with the gas phase, that is, when water is not formed through the direct gas-phase reaction of H₂ and O₂ (see the computed phase diagram in Figure S18 in the Supporting Information). At high oxygen chemical potentials, Cu₂O is thermodynamically stable. As the oxygen chemical potential decreases, the bulk oxide is no longer stable while a series of oxide-like Cu (111) surfaces become stable. The considered phases have a *p* (4 × 4) periodicity.^[46] The most oxidized of these, denoted by *p*4-O_{ads}, can be visualized as hexagonal rings composed of O–Cu–O motifs with oxygen adsorbed in the fcc hollow sites (O_{ads}) inside the hexagonal rings (Figure S18, Supporting Information). As the oxygen chemical potential is reduced, the O_{ads} is destabilized, leaving the bare *p*4 structure, which can further lose oxygen from its surface, at even lower oxygen chemical potentials, until the clean Cu (111) surface becomes stable. However, at the oxygen chemical potentials used in this work, only Cu₂O is predicted to be thermodynamically stable, in agreement with literature data.^[54]

The thermodynamic stability of Cu₂O appears to contradict our experimental observation of formation of metallic copper. However, this apparent discrepancy is likely a consequence of chemical dynamics controlling the catalyst’s surface during the catalytic reaction, in preference to thermodynamics. A simple microkinetic model, taking into account the competition between catalyst oxidation and reduction, can rationalize this experiment result (see Figures S19–S23 and discussions in the Supporting Information) and generate a dynamic stability diagram (Figure 5A). This stability diagram predicts a transformation of Cu₂O into the *p*4-O_{ads} phase at ≈550 °C and at a H₂/O₂ ratio of 10/1 into the *p*4 structure at 750 °C, in reasonable agreement with the experiment. Moreover, the dynamic stability diagram gives a qualitatively different picture than the thermodynamic phase diagram, underlining the importance of considering chemical dynamics during the catalytic operation.

The different surface terminations shown in Figure 5A are also expected to exhibit different catalytic pathways. For the *p*4-O_{ads} surface, our DFT calculations show that hydrogen is oxidized on the oxide-like overlayer through a Langmuir–Hinshelwood (LH)-like mechanism (Figure 5B, right). In this case, additional O accumulates on the oxide-like layer as the system is near the Cu/Cu₂O dynamic transition (Figure 5C,D). This O_{ads} is effective in activating adsorbed H₂ to produce OH_{ads} and H_{ads}, which can readily combine to produce water (Figure S19, Supporting Information). The catalytic cycle is closed by replacement of O_{ads} lost for water formation by dissociated O₂ (Figure S20, Supporting Information). As such, the process competes with the growth of bulk Cu₂O. Conversely, at higher temperature, beyond the dynamic stability limit of bulk Cu₂O, the system does not accommodate the O_{ads} species active in the LH-like mechanism. In this case, water can be produced through a Mars–van Krevelen (MvK)-like mechanism, involving lattice O in the oxide-like layer (Figure 5B, left). While this oxide layer is ineffective in direct H₂ activation (Figure S22, Supporting Information), we note that metallic Cu is present at the particle edges (Figure 5E,F). This metallic surface can activate H₂ and supply H_{ads} to the edges of the oxide-like overlayer via spill over. Water can thus be produced through an MvK-like mechanism at the interface between facets covered by O_{ads} and

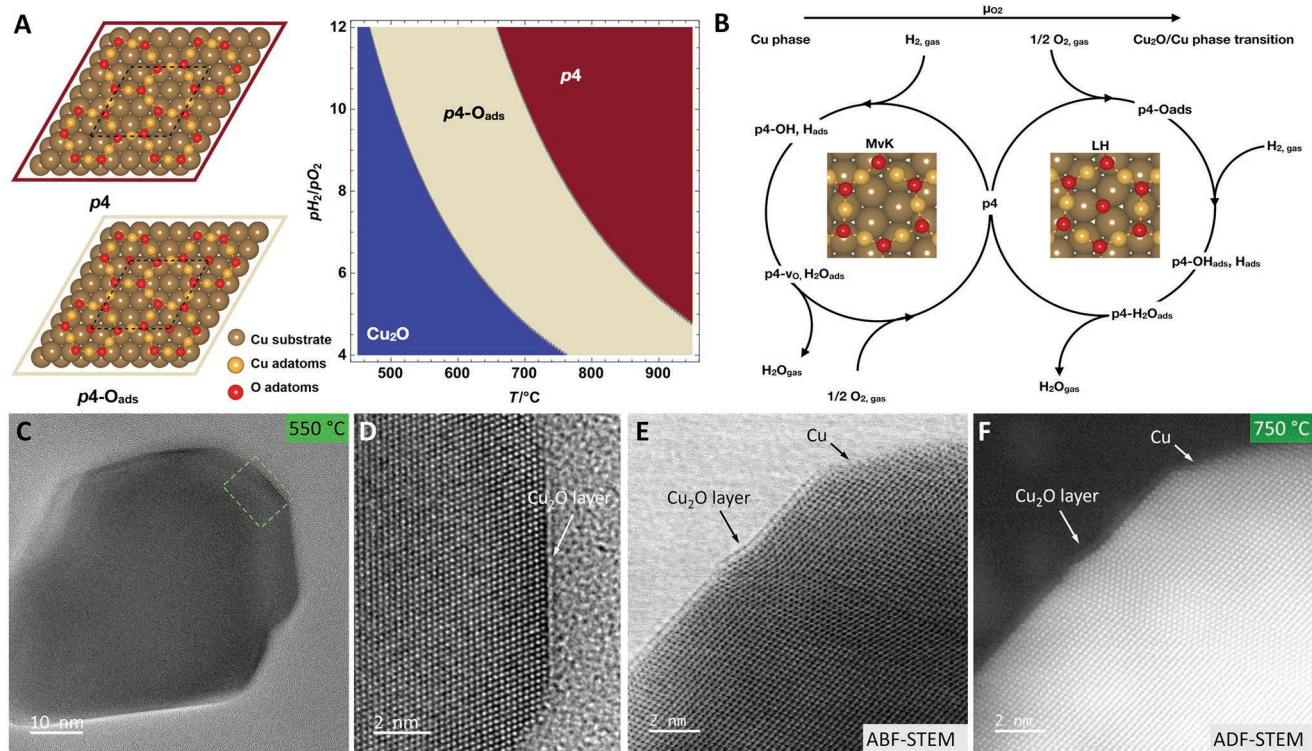


Figure 5. Theoretical calculations. A) Computed p versus T phase diagram for the Cu (111) surface under $H_{2, \text{gas}}$ and $O_{2, \text{gas}}$ at 62.7 mbar total pressure computed with $E_{a, \text{max}}$ (see the Supporting Information for details). B) Reaction pathways of hydrogen oxidation on $p4$ covered Cu (111) surface following the MvK-like mechanism (left) and LH-like mechanism (right) at different temperature regimes. C, D) In situ HRTEM images of a copper nanoparticle recorded at 550 °C (electron dose rate: $3.6 \times 10^5 \text{ e nm}^{-2} \text{ s}^{-1}$). E, F) High-resolution annular bright-field scanning TEM (ABF-STEM) and annular dark-field scanning TEM (ADF-STEM) images recorded at 750 °C ($p_{H_2} = 57 \text{ mbar}$, $p_{O_2} = 5.7 \text{ mbar}$).

uncovered (i.e., metallic) facets (Figure S23, Supporting Information). In situ observations at 750 °C reveal a fluctuating lateral movement of atoms in the overlayer, indicating ongoing redox processes at the edge of the particle (Movie S16, Supporting Information).

It should be noted that while the simulated dynamic stability diagram is drawn with sharp boundaries between the phases, these structures are controlled by surface dynamics with varying coverages of oxygen and hydrogen reacting through the LH- and MvK-like mechanisms. The variable coverages will tend to broaden the dynamic transitions relative to sharp thermodynamic phase boundaries.^[55] This behavior can be observed in the phase coexistence seen experimentally, where both oxide and metal exist under a much wider range of redox conditions than expected for a system under pure thermodynamic control.

2.2. Fundamental Relevance of Redox Dynamics

Having demonstrated particle dynamics for hydrogen oxidation on copper and in an earlier work also for the case of bulk copper foils,^[40] we set about to assess the generality of the phenomena described above. First, we investigated the state of copper under conditions of methanol oxidation, i.e., for a catalytic reaction that is relevant to industrial synthesis of formaldehyde. **Figure 6** shows in situ TEM images of Cu nanoparticles recorded at 600 and 500 °C (Figure 6A–C and 6E–G),

respectively ($p_{\text{MeOH}} = p_{O_2} = 13.1 \text{ mbar}$). The dynamic behavior observed is due to the oscillatory phase transition between Cu^0 and Cu_2O that involves reshaping, sintering, and splitting of particles (Movie S17, Supporting Information), similar to what was observed in the case of hydrogen oxidation. As discussed above, these oscillations are due to chemical dynamics. A shift to a more oxidized state with decreasing temperature was observed and verified by in situ SAED (Figure 6D, H). The redox dynamics are most pronounced at around 500 °C under the chosen 1:1 ratio of MeOH and O_2 . A subtle increase in formaldehyde formation with increasing structural dynamics can be discerned in collected MS data (Figure S24, Supporting Information). Phase coexistence in the active regime agrees with earlier studies in which, however, the associated structural dynamics could not be observed directly.

Next, we investigated methane oxidation on Pd, i.e., a transition metal that is harder to oxidize than Cu (see **Figure 7**). As in the case of copper, structural dynamics evolve when Pd is driven toward the Pd/PdO phase boundary. As expected for a more noble metal, this requires a higher partial pressure of oxygen. In an $\approx 2:1$ ratio of CH_4 and O_2 ($p_{\text{CH}_4} = 50.5 \text{ mbar}$ and $p_{O_2} = 22.4 \text{ mbar}$), the catalyst remains relatively static at 350 °C and shows coexistence of Pd and PdO as evidenced by the in situ SAED. The system evolves to a highly dynamic state at 550 °C (Movie S18, Supporting Information). The MS data recorded simultaneously with TEM observation reveal a pronounced formation of CO_2 and consumption of CH_4 and O_2 under these conditions (Figure 7I).

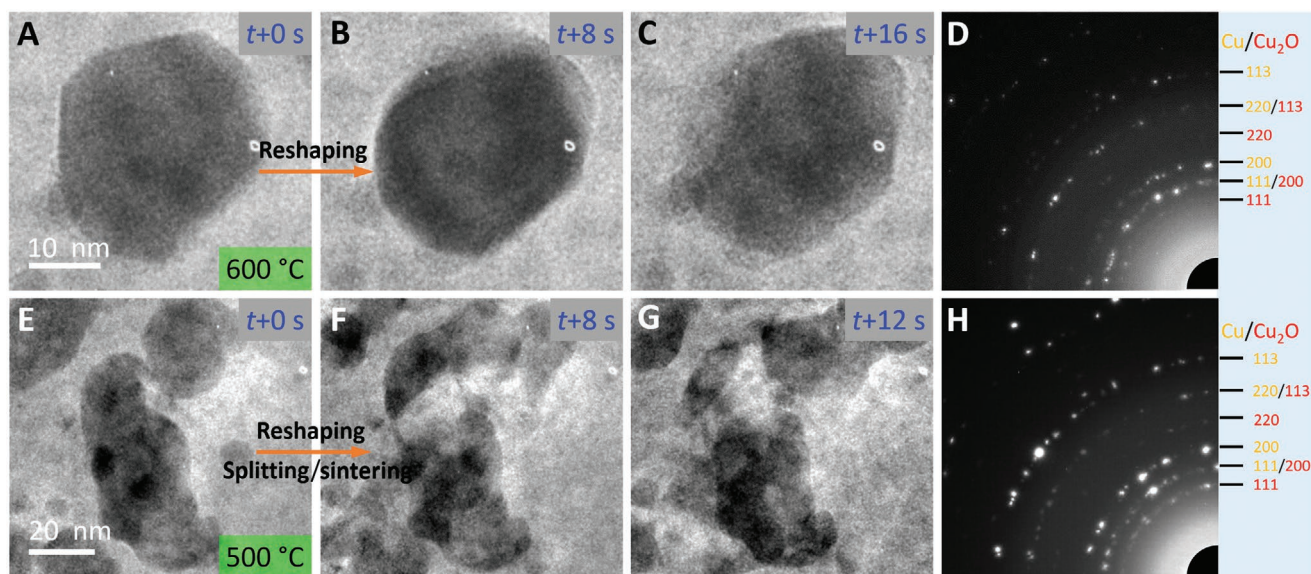


Figure 6. Structural dynamics of Cu in methanol oxidation reaction. A–H) TEM images and SAED patterns of Cu recorded in situ during methanol oxidation at 600 °C (A–D) and at 500 °C (E–H), respectively (electron dose rate $\approx 10^3$ to 10^4 $e\text{ nm}^{-2}\text{ s}^{-1}$; $p_{\text{MeOH}} = 13.1$ mar and $p_{\text{O}_2} = 13.1$ mar). The white dots appearing in (A–C) and (E–G) are due to camera artifacts.

Overall, we have observed oscillatory redox dynamics on the level of individual particles (Cu or Pd) and revealed details of the interplay between coexisting phases. Our results corroborate earlier studies based on integral spectroscopic techniques.^[13,32,33,36] In the absence of coupling between the redox dynamics of individual particles, either through temperature (i.e., thermokinetic oscillations) or through the gas phase, integral spectroscopic data^[13,33,36] or MS data (this work) do not show signs of an oscillatory behavior. There are, however, many reactions in which collective redox oscillation has been detected.^[36,56–59] The emergence of a dynamic behavior even far from a thermodynamic phase boundary, as a result of the interplay between reducing and oxidizing components in the gas phase, is thus a general phenomenon that can occur in metal-catalyzed redox reactions.

3. Conclusion

Using copper as a catalyst and hydrogen oxidation as the most elementary redox reaction, our operando TEM study demonstrates that even a relatively simple reaction can give rise to very complex dynamics. Real-time imaging coupled with on-line mass spectrometry revealed the relation between structural dynamics and associated catalytic activity. The observed dynamics are a consequence of the complementary chemical driving forces of simultaneously presented reducing and oxidizing species. Depending on the chemical potential, different regimes and dominating catalytic mechanisms have been identified. The working state results from the adjustment of the catalyst to the operating conditions. Catalytic function emerges as a consequence of the ongoing competition between reducing and oxidizing potentials with respect to the phase stability of metallic and oxidized portions of the catalyst. While oxidized (i.e., Cu_2O) catalyst shows low activity, structural dynamics

are observed at intermediate temperatures (450–650 °C), in a regime where bulk copper oxide and metallic copper coexist and constantly interconvert owing to the competition between reducing and oxidizing reactants. Oscillatory redox cycling between Cu and Cu_2O coincides with a substantial increase in water formation, indicating oxide reduction as the dominant mechanism for water formation in this regime. The associated structural dynamics involve particle reshaping, sintering, and splitting, and are of importance with regard to our understanding of catalyst sintering. At higher temperatures, structural dynamics cease, except for surface reconstructions and redox processes involving only a monolayer oxide. Supported by DFT calculations, two regimes with dominating LH, and, at even higher temperature, MvK-like mechanisms have been identified. The latter emerges as the monolayer oxide becomes the sole remaining oxygen source for HOR. Finally, the findings obtained for copper in hydrogen oxidation have been extended to other redox reactions such as industrially relevant methanol oxidation on Cu or methane oxidation on Pd.

Overall, our study clearly demonstrates that the state of the working catalyst and, thus, the dominant catalytic mechanism depend strongly on the applied chemical potential. Description of static catalyst particles that can be designed with a specific shape and exposed facets is thus oversimplified, at least in redox reactions. Furthermore, operation of a catalyst at the “sweet spot” is not necessarily achievable at the desired stoichiometric ratio for a particular reaction. The observations also show that all active regimes are characterized by the coexistence of metal and (surface) oxide, explaining the phase coexistence that has been described in earlier studies. While the oscillatory behavior has often been observed in metal-catalyzed redox reactions, our study shows the associated dynamics at the single particle level down to the atomic scale. The emerging picture supports a description of an active catalyst in its surrounding as a driven (redox) oscillator. This view provides a

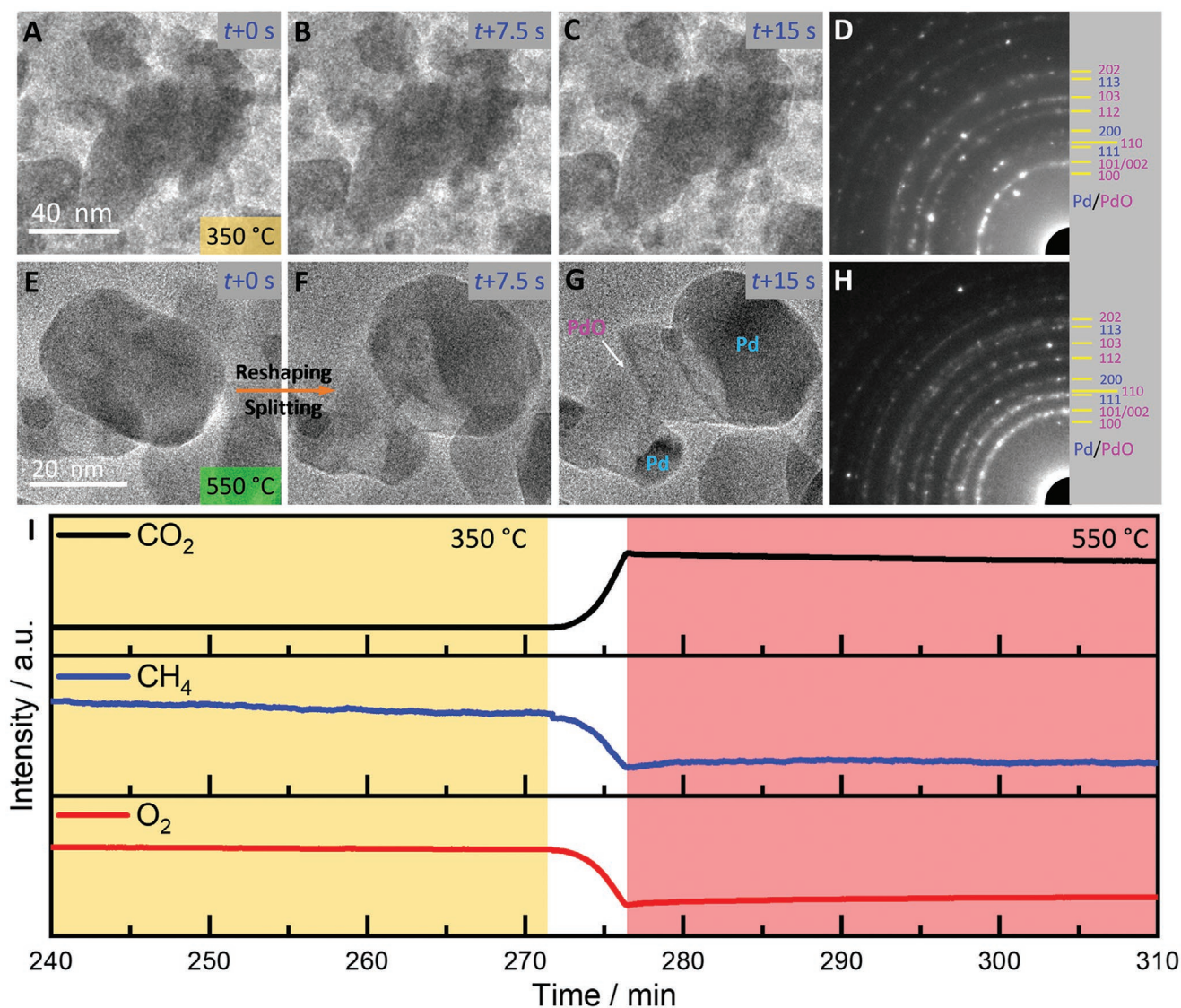


Figure 7. Structural dynamics related to catalytic activity in methane oxidation on Pd. A–H) In situ TEM images and SAED patterns of Pd recorded during methane oxidation ($P_{\text{CH}_4} = 50.5$ mbar and $P_{\text{O}_2} = 22.4$ mbar) at 350 °C (A–D) and 550 °C (E–H), respectively (electron dose rate: $1.2\text{--}4 \times 10^4 e \text{ nm}^{-2} \text{ s}^{-1}$). I) MS data recorded during in situ TEM observation of Pd in methane oxidation.

convenient mechanism for the constant generation and recovery of transient active sites in a system that can appear even far from a thermodynamic phase boundary.

Supporting Information

Supporting Information is available from the Wiley Online Library or from the author.

Acknowledgements

X.H. acknowledges the financial support from ETH Career Seed Grant SEED-14 18-2. M.-G.W. and X.H. acknowledge the funding from the SNF project 200021_181053. The authors also acknowledge Masahiro Hashimoto from JEOL company for his assistance with MS tuning for in situ experiments. Arik Beck is thanked for the discussion of the results.

Conflict of Interest

The authors declare no conflict of interest.

Author Contribution

M.-G.W. initiated the project which was later led by X.H., who performed the in situ TEM experiments and analyzed the data. M.-G.W. carried out the in situ ESEM experiment. R.F. participated in the early stages of the project and performed the in situ experiment of methanol oxidation on Cu. T.J. designed and performed the DFT calculations. X.H. wrote the original draft of the paper. The final version of the manuscript was prepared by X.H. with significant contribution from M.-G.W., A.F., T.J., and C.C. R.S. contributed to the valuable discussion of the work.

Data Availability Statement

Research data are not shared.

Keywords

chemical dynamics, metal catalysts, oscillatory redox dynamics, phase coexistence, phase transitions, structure–activity correlation

Received: March 5, 2021

Revised: April 10, 2021

Published online:

- [1] J. Zhong, X. Yang, Z. Wu, B. Liang, Y. Huang, T. Zhang, *Chem. Soc. Rev.* **2020**, *49*, 1385.
- [2] M. B. Ross, P. De Luna, Y. Li, C.-T. Dinh, D. Kim, P. Yang, E. H. Sargent, *Nat. Catal.* **2019**, *2*, 648.
- [3] M. Behrens, *Angew. Chem., Int. Ed.* **2014**, *53*, 12022.
- [4] M. T. Greiner, T. E. Jones, A. Klyushin, A. Knop-Gericke, R. Schlögl, *J. Am. Chem. Soc.* **2017**, *139*, 11825.
- [5] M. Jayamurthy, P. Hayden, A. K. Bhattacharya, *J. Catal.* **2014**, *309*, 309.
- [6] F. Xu, K. Mudiyansele, A. E. Baber, M. Soldemo, J. Weissenrieder, M. G. White, D. J. Stacchiola, *J. Phys. Chem. C* **2014**, *118*, 15902.
- [7] J. Stötzl, R. Frahm, B. Kimmerle, M. Nachttegaal, J.-D. Grunwaldt, *J. Phys. Chem. C* **2012**, *116*, 599.
- [8] A. Hellman, A. Resta, N. M. Martin, J. Gustafson, A. Trincherio, P. A. Carlsson, O. Balmes, R. Felici, R. van Rijn, J. W. M. Frenken, J. N. Andersen, E. Lundgren, H. Grönbeck, *J. Phys. Chem. Lett.* **2012**, *3*, 678.
- [9] M. Roiaz, E. Monachino, C. Dri, M. Greiner, A. Knop-Gericke, R. Schlögl, G. Comelli, E. Vesselli, *J. Am. Chem. Soc.* **2016**, *138*, 4146.
- [10] T. C. R. Rocha, A. Oestereich, D. V. Demidov, M. Hävecker, S. Zafeirotas, G. Weinberg, V. I. Bukhtiyarov, A. Knop-Gericke, R. Schlögl, *Phys. Chem. Chem. Phys.* **2012**, *14*, 4554.
- [11] M. T. Greiner, J. Cao, T. E. Jones, S. Beeg, K. Skorupska, E. A. Carbonio, H. Sezen, M. Amati, L. Gregoratti, M.-G. Willinger, A. Knop-Gericke, R. Schlögl, *ACS Catal.* **2018**, *8*, 2286.
- [12] F. Zhang, Z. Liu, S. Zhang, N. Akter, R. M. Palomino, D. Vovchok, I. Orozco, D. Salazar, J. A. Rodriguez, J. Llorca, J. Lee, D. Kim, W. Xu, A. I. Frenkel, Y. Li, T. Kim, S. D. Senanayake, *ACS Catal.* **2018**, *8*, 3550.
- [13] B. Eren, C. Heine, H. Bluhm, G. A. Somorjai, M. Salmeron, *J. Am. Chem. Soc.* **2015**, *137*, 11186.
- [14] V. V. Kaichev, D. Teschner, A. A. Saraev, S. S. Kosolobov, A. Y. Gladky, I. P. Prosvirin, N. A. Rudina, A. B. Ayupov, R. Blume, M. Hävecker, A. Knop-Gericke, R. Schlögl, A. V. Latyshev, V. I. Bukhtiyarov, *J. Catal.* **2016**, *334*, 23.
- [15] F. Tao, P. A. Crozier, *Chem. Rev.* **2016**, *116*, 3487.
- [16] B. He, Y. Zhang, X. Liu, L. Chen, *ChemCatChem* **2020**, *12*, 1853.
- [17] E. Ruska, *Kolloid-Z.* **1942**, *100*, 212.
- [18] W. Yuan, B. Zhu, X.-Y. Li, T. W. Hansen, Y. Ou, K. Fang, H. Yang, Z. Zhang, J. B. Wagner, Y. Gao, Y. Wang, *Science* **2020**, *367*, 428.
- [19] H. Yoshida, Y. Kuwauchi, J. R. Jinschek, K. Sun, S. Tanaka, M. Kohyama, S. Shimada, M. Haruta, S. Takeda, *Science* **2012**, *335*, 317.
- [20] X. Sun, W. Zhu, D. Wu, C. Li, J. Wang, Y. Zhu, X. Chen, J. A. Boscoboinik, R. Sharma, G. Zhou, *Nat. Commun.* **2020**, *11*, 305.
- [21] Z. Ma, L. Sheng, X. Wang, W. Yuan, S. Chen, W. Xue, G. Han, Z. Zhang, H. Yang, Y. Lu, Y. Wang, *Adv. Mater.* **2019**, *31*, 1903719.
- [22] S. B. Vendelbo, C. F. Elkjær, H. Falsig, I. Puspitasari, P. Dona, L. Mele, B. Morana, B. J. Nelissen, R. van Rijn, J. F. Creemer, P. J. Kooyman, S. Helveg, *Nat. Mater.* **2014**, *13*, 884.
- [23] P. L. Hansen, J. B. Wagner, S. Helveg, J. R. Rostrup-Nielsen, B. S. Clausen, H. Topsøe, *Science* **2002**, *295*, 2053.
- [24] Y. Jiang, H. Li, Z. Wu, W. Ye, H. Zhang, Y. Wang, C. Sun, Z. Zhang, *Angew. Chem., Int. Ed.* **2016**, *55*, 12427.
- [25] B. K. Miller, P. A. Crozier, *Microsc. Microanal.* **2014**, *20*, 815.
- [26] Y. Niu, X. Liu, Y. Wang, S. Zhou, Z. Lv, L. Zhang, W. Shi, Y. Li, W. Zhang, D. S. Su, B. Zhang, *Angew. Chem., Int. Ed.* **2019**, *58*, 4232.
- [27] L. F. Allard, S. H. Overbury, W. C. Bigelow, M. B. Katz, D. P. Nackashi, J. Damiano, *Microsc. Microanal.* **2012**, *18*, 656.
- [28] J. F. Creemer, S. Helveg, P. J. Kooyman, A. M. Molenbroek, H. W. Zandbergen, P. M. Sarro, *J. Microelectromech. Syst.* **2010**, *19*, 254.
- [29] K. Larmier, W.-C. Liao, S. Tada, E. Lam, R. Verel, A. Bansode, A. Urakawa, A. Comas-Vives, C. Copéret, *Angew. Chem., Int. Ed.* **2017**, *56*, 2318.
- [30] S. Nitopi, E. Bertheussen, S. B. Scott, X. Liu, A. K. Engstfeld, S. Horch, B. Seger, I. E. L. Stephens, K. Chan, C. Hahn, J. K. Nørskov, T. F. Jaramillo, I. Chorkendorff, *Chem. Rev.* **2019**, *119*, 7610.
- [31] D. Gao, R. M. Arán-Ais, H. S. Jeon, B. R. Cuenya, *Nat. Catal.* **2019**, *2*, 198.
- [32] H. Bluhm, M. Hävecker, A. Knop-Gericke, E. Kleimenov, R. Schlögl, D. Teschner, V. I. Bukhtiyarov, D. F. Ogletree, M. Salmeron, *J. Phys. Chem. B* **2004**, *108*, 14340.
- [33] A. Knop-Gericke, M. Hävecker, T. Schedel-Niedrig, R. Schlögl, *Top. Catal.* **2001**, *15*, 27.
- [34] Z. Zhang, S.-S. Wang, R. Song, T. Cao, L. Luo, X. Chen, Y. Gao, J. Lu, W.-X. Li, W. Huang, *Nat. Commun.* **2017**, *8*, 488.
- [35] A. A. Gokhale, J. A. Dumesic, M. Mavrikakis, *J. Am. Chem. Soc.* **2008**, *130*, 1402.
- [36] H. Werner, D. Herein, G. Schulz, U. Wild, R. Schlögl, *Catal. Lett.* **1997**, *49*, 109.
- [37] G. Zhou, L. Luo, L. Li, J. Ciston, E. A. Stach, J. C. Yang, *Phys. Rev. Lett.* **2012**, *109*, 235502.
- [38] L. Zou, J. Li, D. Zakharov, E. A. Stach, G. Zhou, *Nat. Commun.* **2017**, *8*, 307.
- [39] A. P. LaGrow, M. R. Ward, D. C. Lloyd, P. L. Gai, E. D. Boyes, *J. Am. Chem. Soc.* **2017**, *139*, 179.
- [40] J. Cao, A. Rinaldi, M. Plodinec, X. Huang, E. Willinger, A. Hammud, S. Hieke, S. Beeg, L. Gregoratti, C. Colbea, R. Schlögl, M. Antonietti, M. Greiner, M. Willinger, *Nat. Commun.* **2020**, *11*, 3554.
- [41] J. C. Nava Paz, H. J. Grabke, *Oxid. Met.* **1993**, *39*, 437.
- [42] X. Duan, O. Warschkow, A. Soon, B. Delley, C. Stampfl, *Phys. Rev. B* **2010**, *81*, 075430.
- [43] M. V. Twigg, M. S. Spencer, *Top. Catal.* **2003**, *22*, 191.
- [44] T. W. Hansen, A. T. DeLaRiva, S. R. Challa, A. K. Datye, *Acc. Chem. Res.* **2013**, *46*, 1720.
- [45] L. Zeng, Z. Cheng, J. A. Fan, L.-S. Fan, J. Gong, *Nat. Rev. Chem.* **2018**, *2*, 349.
- [46] A. Soon, M. Todorova, B. Delley, C. Stampfl, *Phys. Rev. B* **2006**, *73*, 165424.
- [47] R. Feidenhans'l, F. Grey, M. Nielsen, F. Besenbacher, F. Jensen, E. Laegsgaard, I. Stensgaard, K. W. Jacobsen, J. K. Nørskov, R. L. Johnson, *Phys. Rev. Lett.* **1990**, *65*, 2027.
- [48] H. Iddir, D. D. Fong, P. Zapol, P. H. Fuoss, L. A. Curtiss, G. W. Zhou, J. A. Eastman, *Phys. Rev. B* **2007**, *76*, 241404.
- [49] F. Jensen, F. Besenbacher, E. Laegsgaard, I. Stensgaard, *Surf. Sci. Lett.* **1991**, *259*, L774.
- [50] W. Liu, K. C. Wong, K. A. R. Mitchell, *Surf. Sci.* **1995**, *339*, 151.
- [51] W. Liu, K. C. Wong, H. C. Zeng, K. A. R. Mitchell, *Prog. Surf. Sci.* **1995**, *50*, 247.
- [52] T. Schedel-Niedrig, T. Neisius, I. Böttger, E. Kitzelmann, G. Weinberg, D. Demuth, R. Schlögl, *Phys. Chem. Chem. Phys.* **2000**, *2*, 2407.
- [53] A. J. Nagy, G. Mestl, D. Herein, G. Weinberg, E. Kitzelmann, R. Schlögl, *J. Catal.* **1999**, *182*, 417.
- [54] H. Amekura, O. A. Plaksin, K. Kono, Y. Takeda, N. Kishimoto, *J. Phys. D: Appl. Phys.* **2006**, *39*, 3659.
- [55] K. Reuter, M. Scheffler, *Phys. Rev. B* **2003**, *68*, 045407.
- [56] X. Zhang, D. O. Hayward, D. M. P. Mingos, *Catal. Lett.* **2002**, *83*, 149.
- [57] F. Schüth, B. E. Henry, L. D. Schmidt, *Adv. Catal.* **1993**, *39*, 51.
- [58] V. V. Kaichev, A. Y. Gladky, A. A. Saraev, S. S. Kosolobov, O. V. Sherstyuk, V. I. Bukhtiyarov, *Top. Catal.* **2020**, *63*, 24.
- [59] X. Zhang, C. S. M. Lee, D. M. P. Mingos, D. O. Hayward, *Appl. Catal., A* **2003**, *240*, 183.